

Edge Shear Flows and Particle Transport near the Density Limit of the HL-2A Tokamak

R. Hong,¹ G. R. Tynan,^{1,3} P. H. Diamond,^{2,3} L. Nie,³ D. Guo,³ T. Long,³
R. Ke,^{3,4} Y. Wu,^{3,5} B. Yuan,^{3,5} M. Xu,³ and the HL-2A Team³

¹*Center for Energy Research, University of California San Diego, La Jolla, CA 92093, USA*

²*Center for Astrophysics and Space Sciences,
University of California San Diego, La Jolla, CA 92093, USA*

³*Center for Fusion Sciences, Southwestern Institute
of Physics, Chengdu, Sichuan 610041, China*

⁴*Department of Engineering Physics,
Tsinghua University, Beijing 100084, China*

⁵*School of Nuclear Science and Technology,
University of Science and Technology of China, Hefei, Anhui 230026, China*

(Dated: December 14, 2024)

Abstract

Edge shear flow and its effect on regulating turbulent transport have long been suspected to play an important role in plasmas operating near the Greenwald limit n_G . In this study, equilibrium profiles as well as the turbulent particle flux and Reynolds stress across the separatrix in the HL-2A tokamak are examined as n_G is approached in ohmic L-mode discharges. As the normalized line-averaged density \bar{n}_e/n_G is raised, the electron density and pressure gradient increase, and the electron temperature flattens. The shearing rate of the poloidal $\mathbf{E} \times \mathbf{B}$ and turbulent phase velocities drop. Also, turbulent particle transport increases in high collisionality plasmas. The turbulent drive for the low-frequency zonal flow (the Reynolds power) collapses at higher \bar{n}_e/n_G values, while the geodesic acoustic modes (GAMs) gain more energy in higher density plasmas. But the shearing rate of GAMs is less than low-frequency zonal flows, i.e. $\omega_{\text{GAM}} \sim 0.3 \times \omega_{\text{sh}}$, indicating that zonal flows play leading role in turbulence suppression. Besides damping the edge shear flows through increased collisional dissipation, the increased collisionality can also be connected to an increased non-adiabatic electron response at high densities, which raises the cross-correlation between density and potential perturbations. Moreover, enhanced particle transport can be incorporated into radiation models to explain strong MHD instabilities and disruptions when the Greenwald limit is exceeded.

I. INTRODUCTION

High density operations are desirable in magnetic confinement fusion reactors. Densities of the order of 10^{20} m^{-3} are required for achieving ignition [1–3]. However, raising the line-averaged density, \bar{n}_e , to the Greenwald limit, $n_G [10^{20} \text{ m}^{-3}] = \frac{I_p[\text{MA}]}{\pi a^2[\text{m}^2]}$, usually leads to a significant reduction in confinement time, or even disruption, when n_G is exceeded [2, 4]. Since the discovery of this density limit, extensive experimental studies have shown that the Greenwald limit can be exceeded by increasing the core density while keeping the edge density low, i.e. by operating with peaked density profiles, using optimized fueling techniques [5–8]. These findings provide strong evidence linking the density limit to the edge physics [2].

Among the phenomena in the plasma boundary region, edge cooling and radiation loss are found to be associated with the density limit, and have been widely investigated [2, 4, 9, 10]. In radiation models [2, 11], the radiative heat loss due to increased impurity content in the plasma is thought to dominate the power balance at high densities, resulting in strong edge cooling and thus an increased resistivity, causing the toroidal current channel to shrink. The current shrinkage then leads to an increased current density gradient and the onset of resistive MHD instabilities. In particular, a thermo-resistive tearing mode model [12–14], in which radiative cooling is balanced with the ohmic heating inside magnetic islands, has been invoked to explain the dependence of the current density in the Greenwald limit scaling.

Although radiation models have achieved some success in explaining the empirical scaling, they do not address the mechanism that initiates edge cooling. One likely candidate is enhanced edge transport, i.e. turbulent particle and heat fluxes [2]. We also note that enhanced particle transport has been observed in advance of any change in the MHD activity in both experiments and numerical simulations in high density plasmas [15–19]. At fixed pressure, the higher density usually implies reduced temperature and hence increases dissipative and resistive effects. These effects destabilize the resistive modes, which lead to enhanced fluctuation levels and turbulent transport [20]. Also, turbulent transport can be suppressed or mitigated by zonal flows that are in turn driven by the turbulence via the Reynolds force [21–28]. This self-regulating process has been recognized as an important mechanism for the L – H transition that leads to the edge transport barrier and improved plasma confinement [29–33]. However, zonal flows are subject to strong collisional damping

in high density plasmas [21]. Weaker zonal flows cannot efficiently trigger the "tilt-stretch-absorption" process [24, 26], and therefore result in reduced Reynolds force. As a result, the self-regulation process is inhibited when the density limit is approached, and edge turbulent fluxes should increase. We suggest that the competition between collisionality triggered instabilities and the stabilizing effects of $\mathbf{E} \times \mathbf{B}$ shear flows may lead to the limit of pedestal density.

Studies of turbulent transport in the scrape-off layer (SOL) as \bar{n}_e is raised to the Greenwald limit have shown a pronounced increase in SOL turbulence intermittency [17, 18], demonstrating that turbulent transport undergoes important changes as the density limit is approached. However, as of now, to our knowledge, the evolution of the turbulent particle and momentum fluxes, zonal flows and GAMs, and their interactions across the SOL, separatrix and edge plasma region have not been reported.

In present study we examine the behavior of the edge shear flows and cross-field particle transport as \bar{n}_e approaches the Greenwald limit in ohmic HL-2A tokamak plasmas. The discharges and the diagnostic tools used for this work are discussed in section II. The experimental results and discussions on the evolution of edge shear flows, the nonlinear energy transfer, and the edge particle transport are presented in section III and IV, respectively. A summary of this work is given in section V.

II. EXPERIMENTAL ARRANGEMENT

The experiment was carried out in the HL-2A tokamak [25, 34, 35], which has a major radius of $R = 1.65$ m and a minor radius of $a = 0.4$ m. In this study ohmic L-mode discharges were produced in the lower-single-null (LSN) geometry with the 'favorable' $\nabla\mathbf{B} \times \mathbf{B}$ drift direction (toward the X-point). The plasma current was $I_p = 150$ kA, the toroidal magnetic field was $B_T = 1.3$ T, and the edge safety factor was about $3.5 - 4$. The Greenwald limit density was $n_G = I_p/\pi a^2 \approx 3.2 \times 10^{19}$ m⁻³ in these conditions. In this shot-by-shot density scanning experiment, the line-averaged densities \bar{n}_e measured by the HCN laser interferometer ramped from 0.8×10^{19} to 2.8×10^{19} m⁻³ which correspond to a normalized density range of $0.25 - 0.9 n_G$.

A multi-tip Langmuir probe array was used to investigate the edge turbulence and shear flows at the low-field-side (LFS) mid-plane of the tokamak [25]. The probe is composed of a

3×5 array of graphite tips, i.e. 5 steps with 3 tips on each step. The distance between two adjacent tips is 5 mm in the poloidal direction and 2.5 mm in the radial direction. Tips on the first, the third, and the fifth step were operated as triple probes, providing the electron density n_e and temperature T_e , as well as the plasma potential $\phi_p = \phi_f + 2.8T_e$. Other tips were used to measure the floating potentials ϕ_f . All probe data were sampled at 1 MHz using 12-bit digitizers. With this probe setup, we are also able to simultaneously measure the Reynolds stress, $-\langle \tilde{E}_r \tilde{E}_\theta \rangle / B^2$, and the turbulent particle flux, $\Gamma_r = \langle \tilde{n}_e \tilde{E}_\theta \rangle / B$, where $\tilde{E} = -\nabla \tilde{\phi}_f$.

III. RESULTS

A. Equilibrium Profiles

Figure 1 shows the equilibrium profiles of the electron density n_e , electron temperature T_e , electron pressure $P_e = n_e T_e$, and radial electric field $E_r = -\partial_r \phi_p$ at three different normalized densities, i.e. $\bar{n}_e / n_G \approx 0.3, 0.6$ and 0.8 . These profiles are obtained by taking the time average with 2 millisecond windows. As the normalized core density, \bar{n}_e / n_G , is raised from 0.3 to 0.8, the edge electron density increases by a factor of 3 at a position about 2 cm inside the separatrix, while the electron temperature drops from about 60 eV to 30 eV. Meanwhile, the electron pressure and its radial gradient increase with \bar{n}_e / n_G . The peak value of the radial electric field is reduced (Fig. 1(d)) due to the flattening of the plasma potential profiles at higher \bar{n}_e / n_G values.

B. Kinetic Energy Transfer Analysis

The poloidal phase velocity of plasma fluctuations, $\langle v_\theta \rangle$ (Fig. 3(a)), can be inferred using the time-delay estimation (TDE) technique from two poloidally separated floating potential signals [25]. Here, a pair of 2 msec long time series are used to evaluate the local dispersion relations, i.e. conditional power spectra $S(k_\theta | f) = \frac{S(k_\theta, f)}{\sum_{k_\theta} S(k_\theta, f)}$ at each position (Fig. 2), introducing a spatial resolution of 1 mm (with a 50% overlap). This corresponds to the distance over which the probe tips move during the 2 msec window. The high-frequency fluctuations appear to propagate in the electron diamagnetic drift (EDD) direction inside the separatrix and propagate in the ion diamagnetic drift (IDD) direction in the SOL region.

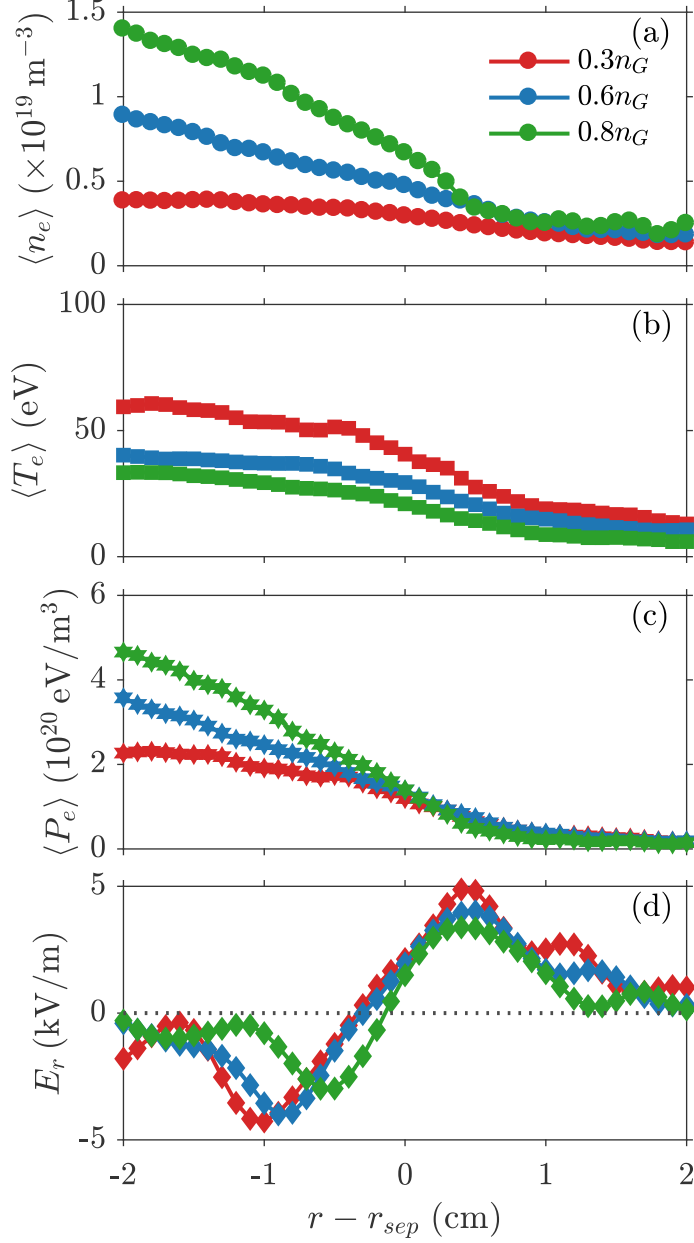


FIG. 1. Equilibrium profiles of the electron density (a), electron temperature (b), electron pressure (c) and radial electric field (d), at three normalized line-averaged densities \bar{n}_e .

When \bar{n}_e/n_G is raised, $\langle v_\theta \rangle$ decreases, particularly in the SOL region. In addition, as shown in Fig. 3(b), the turbulent Reynolds stress (with \tilde{v}_θ and \tilde{v}_r in the frequency range of $20 < f < 100$ kHz), collapses at higher \bar{n}_e/n_G values, leading to a reduced Reynolds force $\mathcal{F}_{Re} = -\partial_r \langle \tilde{v}_\theta \tilde{v}_r \rangle$. The Reynolds power $\mathcal{P}_{Re} = -\langle v_\theta \rangle \partial_r \langle \tilde{v}_\theta \tilde{v}_r \rangle$ (Fig. 3(c)) can also be calculated, which represents the nonlinear kinetic energy transferred from the turbulence into the shear flow. Note here that this quantity looks at the net transfer of kinetic energy from the 20-100

kHz turbulent fluctuations into the low-frequency poloidal velocity ($f < 0.5$ kHz). The peak value of the Reynolds power decreases significantly, when \bar{n}_e/n_G is increased from 0.3 to 0.8, indicating a decline in the nonlinear energy transfer from the turbulence to the edge shear flow. The changes in turbulent Reynolds stress can be also seen in Fig. 4 that shows the joint probability density functions (PDFs) of radial and azimuthal velocities, $\mathbb{P}(\tilde{v}_r, \tilde{v}_\theta)$, at a position of $r - r_{sep} = -2$ cm, at different normalized plasma densities. The tilting angle of the joint PDF decreases as \bar{n}_e/n_G is raised, indicating a reduced anisotropy in the orientation of eddies.

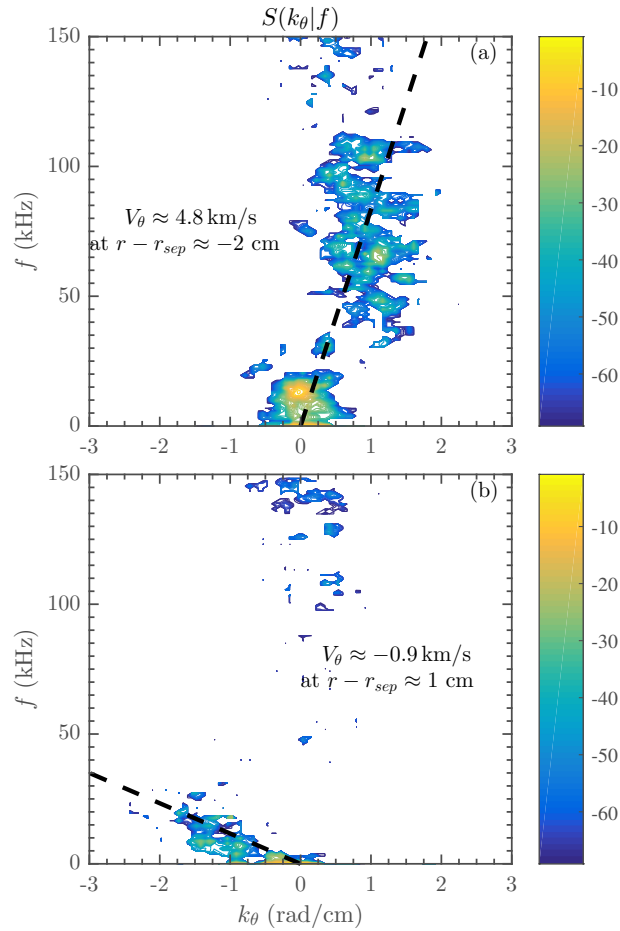


FIG. 2. A typical conditional spectra $S(k_\theta|f)$ at $r - r_{sep} \approx -2$ cm (a) and 1 cm (b), when $\bar{n}_e/n_G \approx 0.6$. Black dash lines imply the local dispersion relations. The positive k_θ is in electron diamagnetic drift (EDD) direction and negative in ion diamagnetic drift (IDD) direction.

Since the edge gradients provide free energy to the turbulence, it would be natural to seek the relation between relevant local gradients and the spatially averaged Reynolds power,

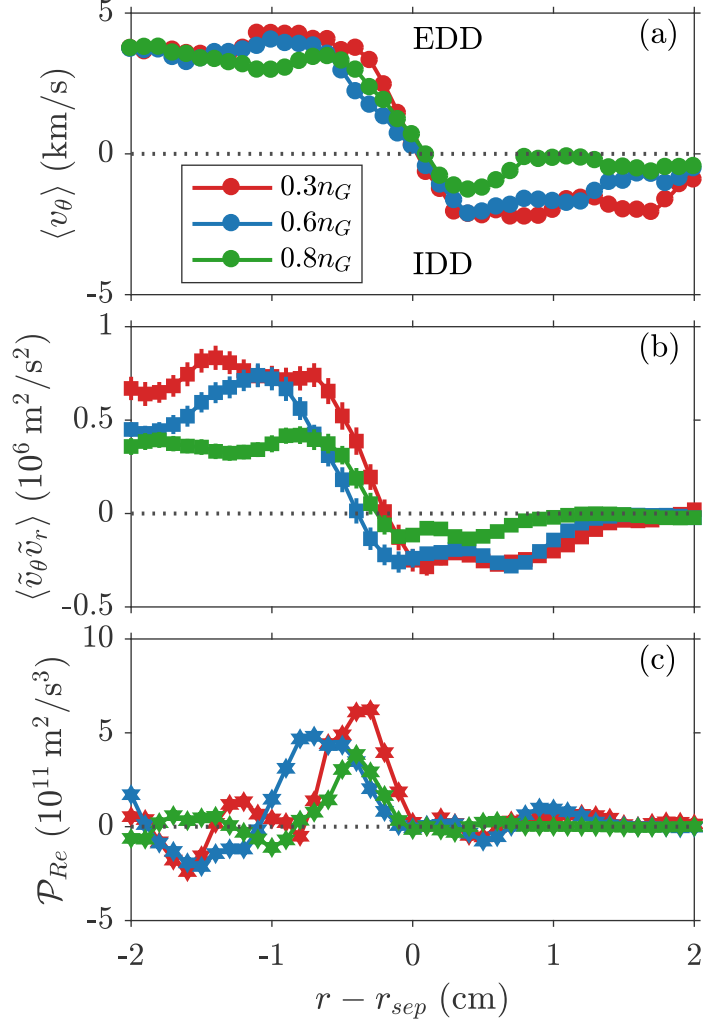


FIG. 3. Profiles of the poloidal phase velocity $\langle v_\theta \rangle$ (a), turbulent Reynolds stress $\langle \tilde{v}_\theta \tilde{v}_r \rangle$ (b) and Reynolds power $\mathcal{P}_{Re} = -\langle v_\theta \rangle \partial_r \langle \tilde{v}_\theta \tilde{v}_r \rangle$ (c), at three normalized line-averaged densities \bar{n}_e/n_G . The positive $\langle v_\theta \rangle$ is in electron diamagnetic drift (EDD) direction and negative $\langle v_\theta \rangle$ in ion diamagnetic drift (IDD) direction.

$\mathcal{P}_{Re}^{av} = \int \mathcal{P}_{Re} r dr / \int r dr$, where the integration is over $-1 < r - r_{sep} < 1$ cm. Figure 5 shows the averaged Reynolds power as a function of edge gradients: (a) normalized electron pressure gradient, $L_{P_e}^{-1} = d_r \ln P_e$; (b) normalized density gradient $L_{n_e}^{-1} = d_r \ln n_e$; (c) normalized electron temperature gradient, $L_{T_e}^{-1} = d_r \ln T_e$; (d) mean shearing rate of poloidal velocity, $\omega_{sh} \approx \left| \frac{\partial \langle v_\theta \rangle}{\partial r} \right|$. While it is not sensitive to the changes in the temperature gradient, \mathcal{P}_{Re}^{av} decreases as $L_{n_e}^{-1}$ is increased, implying a suppression of the nonlinear energy transfer from the turbulence to the low-frequency shear flow at higher densities.

As shown in Fig. 6, the shearing rate of the poloidal flow ω_{sh} decreases when the collision

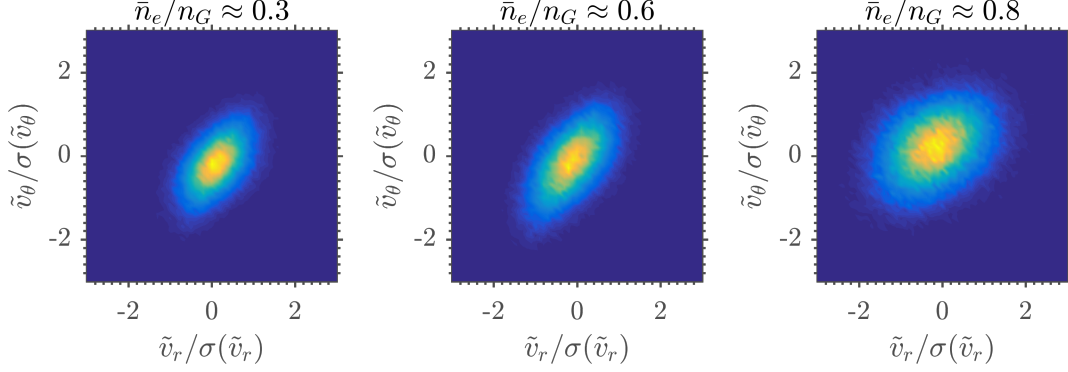


FIG. 4. Joint PDF of radial and azimuthal velocities, $\mathbb{P}(\tilde{v}_r, \tilde{v}_\theta)$, at $r - r_{\text{sep}} = -2$ cm at three densities. Velocities are normalized by their standard deviations.

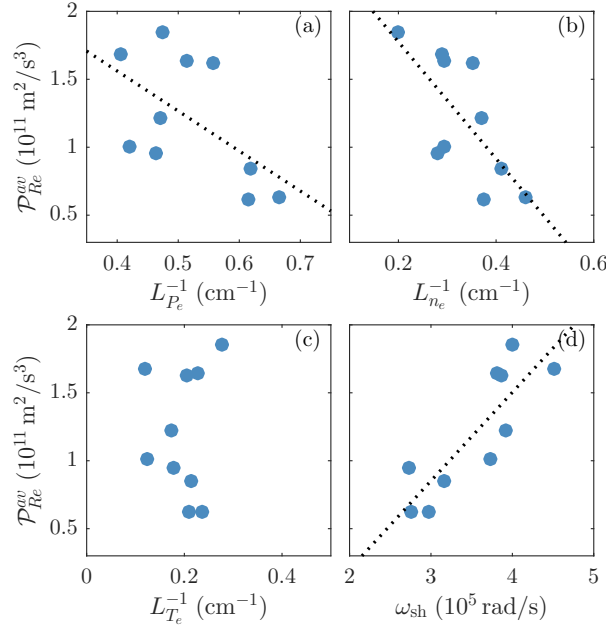


FIG. 5. Averaged Reynolds powers, $\mathcal{P}_{Re}^{av} = \int \mathcal{P}_{Re} r dr / \int r dr$ where $-1 < r - r_{\text{sep}} < 1$ cm, compare against the normalized pressure gradient L_{Pe}^{-1} (a), the normalized density gradient L_{ne}^{-1} (b), the normalized electron temperature gradient L_{Te}^{-1} (c), and the shearing rate of poloidal velocity (d). Black dotted lines imply the linear trends.

rate of either ions or electrons is raised. Here, electron and ion collision rates are spatially averaged over $-1 < r - r_{\text{sep}} < 1$ cm. They are calculated respectively via $\nu_e = 2.91 \times 10^{-6} n T_e^{-3/2} \ln \Lambda$ and $\nu_i = 4.8 \times 10^{-8} Z^4 \mu^{-1/2} n T_i^{-3/2} \ln \Lambda$, with the approximation of $T_i \approx T_e$, where Z is the charge number, μ is the ion mass number, and $\ln \Lambda$ is the Coulomb logarithm, which is 13.6 for electrons and 6.8 for ions. This phenomenon conforms to the

prediction [21, 36] that stronger Coulomb collisions damp zonal flows at higher collisionality. Correspondingly, the averaged Reynolds power \mathcal{P}_{Re}^{av} decreases with increased collision rates (Fig. 7), indicating that the nonlinear energy transfer from the turbulence to the edge shear flow is reduced at higher density and collisionality.

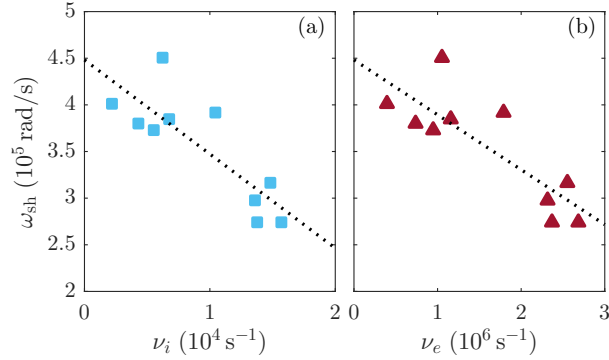


FIG. 6. The flow shearing rate, ω_{sh} , compares against the ion collision rate ν_i (a) and the electron collision rate ν_e (b). Black dotted lines imply the linear trends.

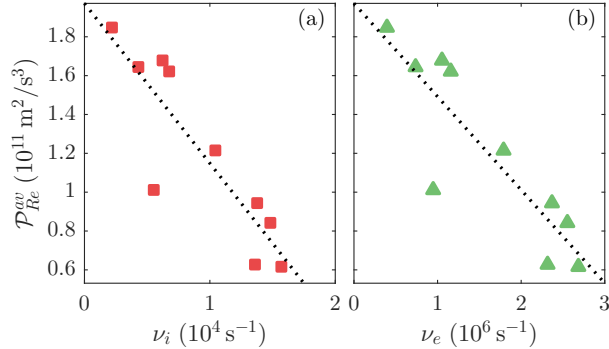


FIG. 7. The averaged Reynolds power, \mathcal{P}_{Re}^{av} , compares against the ion collision rate ν_i (a) and electron collision rate ν_e (b). Black dotted lines imply the linear trends.

The kinetic energy transfer between the edge turbulence and shear flows has also been investigated in the frequency domain. In the auto-spectra of perpendicular velocities $v_{\perp}(f)$ (Fig. 8(a)), at least two distinct flow patterns can be recognized, which are geodesic acoustic modes (GAMs) (centered at $f \approx 12$ kHz) and the turbulence ($f > 30$ kHz). These two patterns have been observed in previous experiments in this device [25, 37, 38]. While there is no obvious changes in the spectra of turbulent velocities, the power contained in GAMs velocity fluctuations increases by a factor of three as \bar{n}_e/n_G is raised from 0.3 to 0.8.

The 2D frequency-resolved nonlinear energy transfer for $\bar{n}_e/n_G = 0.3$ and 0.8 are shown in Fig. 9, which are computed from 100 ensembles of time-stationary data taken roughly at $r - r_{\text{sep}} = -2$ cm. A positive value (red) at (f, f_1) suggests that the perpendicular velocity fluctuations associated with f gain kinetic energy from fluctuations at f_1 ; a negative value (blue) suggests that the fluctuations at f lose energy to those at f_1 . As shown in Fig. 9, the GAMs (at $f \approx 12$ kHz) gain energy from high-frequency fluctuations ($f \approx 40 - 100$ kHz). Figure 8(b) shows the net frequency-resolved nonlinear energy transfer rate [25, 39], $\mathcal{T}_v(f) = -\text{Re} \sum_{f_1} \langle \mathbf{v}_{\perp, f}^* \cdot (\mathbf{v}_{\perp, f-f_1} \cdot \nabla_{\perp} \mathbf{v}_{\perp, f_1}) \rangle$, at different \bar{n}_e/n_G values, which can be obtained by integrating over f_1 axis in the 2D nonlinear energy transfer map. The GAMs appear to gain more kinetic energy from the turbulent fluctuations when \bar{n}_e/n_G is higher. By normalizing the energy transfer rate using auto-power of perpendicular velocity fluctuations, we can obtain the effective frequency-resolved nonlinear growth or damping rate (Fig. 8(c)), $\gamma_{\text{NL}}(f) = \mathcal{T}_v(f) / \langle \tilde{v}_{\perp}^2(f) \rangle$. As shown in Fig. 8(c), the effective nonlinear growth rate of GAMs, $\gamma_{\text{NL}}^{\text{GAM}}$, increased significantly as \bar{n}_e/n_G is raised.

Meanwhile, the shearing rate of GAMs can be estimated using $\omega_{\text{GAM}} = \partial_r v_{\theta}(f = f_{\text{GAM}})$. As shown in Fig. 10, the mean value of ω_{GAM} 's envelope increases from 7 to $10 \times 10^4 \text{ s}^{-1}$ when \bar{n}_e/n_G increases from 0.3 to 0.8 . Also, the eddy turn-over rate is estimated as $\omega_{\text{eddy}} = \tau_{\text{eddy}}^{-1} \sim \frac{\tilde{\phi}_f}{BL_r L_{\theta}} \sim 4.6 - 12 \times 10^4 \text{ s}^{-1}$, where $B = 1.3$ T is the toroidal field, and $\tilde{\phi}_f \sim 30 - 50$ V is the fluctuation amplitude of floating potentials, and $L_r \sim 1$ cm and $L_{\theta} \sim 3 - 5$ cm are respectively the turbulent eddy sizes in radial and poloidal directions [25, 38]. While the shearing rate of GAMs is comparable to the eddy turn-over rate at higher densities, i.e. $\omega_{\text{GAM}} \sim \omega_{\text{eddy}}$, it is still less than the mean flow shearing rate, i.e. $\omega_{\text{GAM}} \sim 0.3 \times \omega_{\text{sh}}$. This indicates that, although GAMs are able to affect the turbulence saturation level and the turbulence dynamics, mean flow plays the leading role in turbulence suppression.

C. Enhanced Particle Flux

Figure 11(a) shows the radial profiles of particle flux at three normalized core densities. The turbulent particle flux, $\Gamma_r = \langle \tilde{n}_e \tilde{v}_r \rangle$, increases substantially when \bar{n}_e/n_G is raised from 0.3 to 0.8 , in spite of the increase of GAMs amplitudes. The root-mean-square (RMS) of the density and radial velocity fluctuations ($20 < f < 100$ kHz) are shown in Fig. 11(b) and 11(c), respectively. While the variation in RMS of radial velocity fluctuations $|\tilde{v}_r|$ is

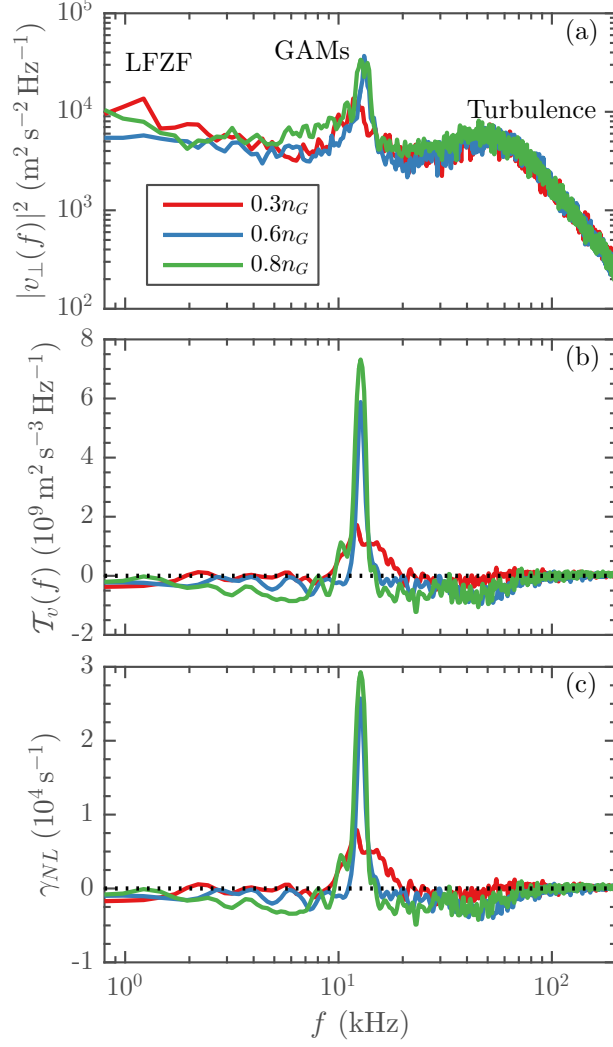


FIG. 8. Auto-spectra of perpendicular velocity fluctuations (a), the nonlinear kinetic energy transfer rate $\mathcal{T}_v(f)$ (b), and the effective growth rate due to energy transfer $\gamma_{NL} = \mathcal{T}_v(f)/\langle \tilde{v}_{\perp}^2(f) \rangle$ (c), at three normalized densities \bar{n}_e/n_G , at a position of $r - r_{\text{sep}} \approx -2$ cm.

negligible, the RMS of electron density fluctuations $|\tilde{n}_e|$ grows twofold as the core density is increased. The cross-phase at each position between \tilde{n}_e and \tilde{v}_r can be evaluated via $\varphi_{n_e, v_r}(f) = \arctan \frac{\text{Im } S_{n_e, v_r}(f)}{\text{Re } S_{n_e, v_r}(f)}$, where $S_{n_e, v_r}(f)$ is the cross-power spectra between \tilde{n}_e and \tilde{v}_r . The cosine of the cross-phase indicates the cross-correlation between these two signals. By integrating over $20 < f < 100$ kHz, we can obtain the profile of the cross-correlation $\cos \varphi_{n_e, v_r}$ (Fig. 11(d)), which increases with \bar{n}_e/n_G values inside the separatrix. Moreover, the cross-phase between density and floating potential fluctuations, $\varphi_{n_e, \phi}$ (Fig. 11(e)), also increases slightly as the plasma density is raised.

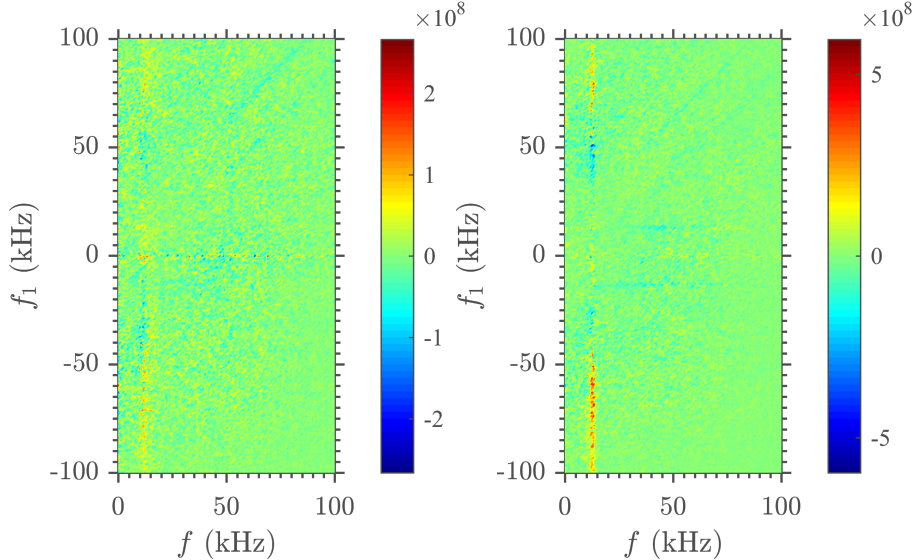


FIG. 9. 2D nonlinear kinetic energy transfer for $\bar{n}_e/n_G \approx 0.3$ (left) and 0.8 (right). A positive value (red) at (f, f_1) means that the perpendicular velocity fluctuations, v_\perp , associated with f gain kinetic energy from those at f_1 ; a negative value (blue) means v_\perp at f lose energy to those at f_1 .

In Fig. 12 the averaged particle flux $\langle \Gamma_r \rangle$ inside the separatrix ($-2 < r - r_{\text{sep}} < 0$ cm) is plotted as the function of edge gradients: (a) normalized pressure gradient $L_{P_e}^{-1}$; (b) normalized density gradient $L_{n_e}^{-1}$; (c) normalized electron temperature gradient $L_{T_e}^{-1}$; (d) mean shearing rate of poloidal velocity. While increasing with $L_{P_e}^{-1}$ and $L_{n_e}^{-1}$, the particle flux $\langle \Gamma_r \rangle$ decreases at higher ω_{sh} which corresponds to lower density.

The $\langle \cos \varphi_{n_e, v_r} \rangle$ and normalized RMS of density fluctuations, $\langle \tilde{n}_e^2 \rangle^{1/2} / \langle n_e \rangle$, are compared against the four edge gradients respectively in Fig. 13 and 14. Both of them increase with $L_{P_e}^{-1}$ and $L_{n_e}^{-1}$, and drop at larger the mean shearing rate ω_{sh} . while the increase in $\langle \cos \varphi_{n_e, v_r} \rangle$ is about 40%, the $\langle \tilde{n}_e^2 \rangle^{1/2} / \langle n_e \rangle$ increases about 200%, showing that the growth in density fluctuation amplitude plays a major role in enhanced particle transport.

IV. DISCUSSION

A. Reduced Shear Flows and Enhanced Particle Transport

In our measurements, the shearing rate of edge mean flows decreases at higher densities. The reduction in edge $\langle E_r \rangle$ shear, as \bar{n}_e/n_G is raised, has also been reported by 3-dimensional fluid simulations of the plasma boundary regions [40], in which the radial

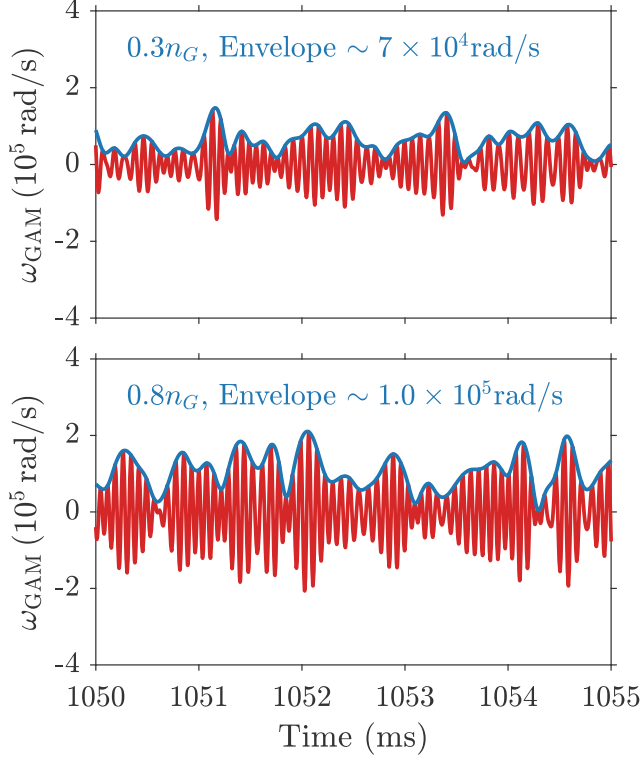


FIG. 10. The shearing rate of GAMs, ω_{GAM} , for $\bar{n}_e/n_G \approx 0.3$ (left) and 0.8 (right). Blue curves indicate envelopes of ω_{GAM} . The mean values of envelopes are $\sim 7 \times 10^4$ rad/s for $\bar{n}_e/n_G \approx 0.3$ and $\sim 10 \times 10^4$ rad/s for $\bar{n}_e/n_G \approx 0.8$.

electric well broadens at higher densities. These findings agree with theoretical considerations [21] and numerical simulations [36] that shear flows are subject to collisional damping effects.

It has been known that strong shear flows are able to tilt and stretch the turbulent eddies, creating the anisotropy to stimulate the Reynolds force that amplifies the zonal flows (ZFs) [21, 24, 26, 27]. This self-regulating process couples the energy of the turbulence to the zonal flow, reducing the amplitude of high-frequency fluctuations that drive turbulent transport. In this study, as the mean flow shear decreases at higher densities, the turbulent Reynolds stress is observed to flatten, leading to reduced Reynolds force and nonlinear energy transfer. The Reynolds force is also negligible in the SOL region. Meanwhile, the tilting angle of the joint PDF of radial and poloidal velocities $\mathbb{P}(\tilde{v}_r, \tilde{v}_\theta)$ decreases, implying that the eddy-tilting process is inhibited when the Greenwald limit is approached.

With the collapsed mean flow shear, enhanced particle transport is also observed. Notice-

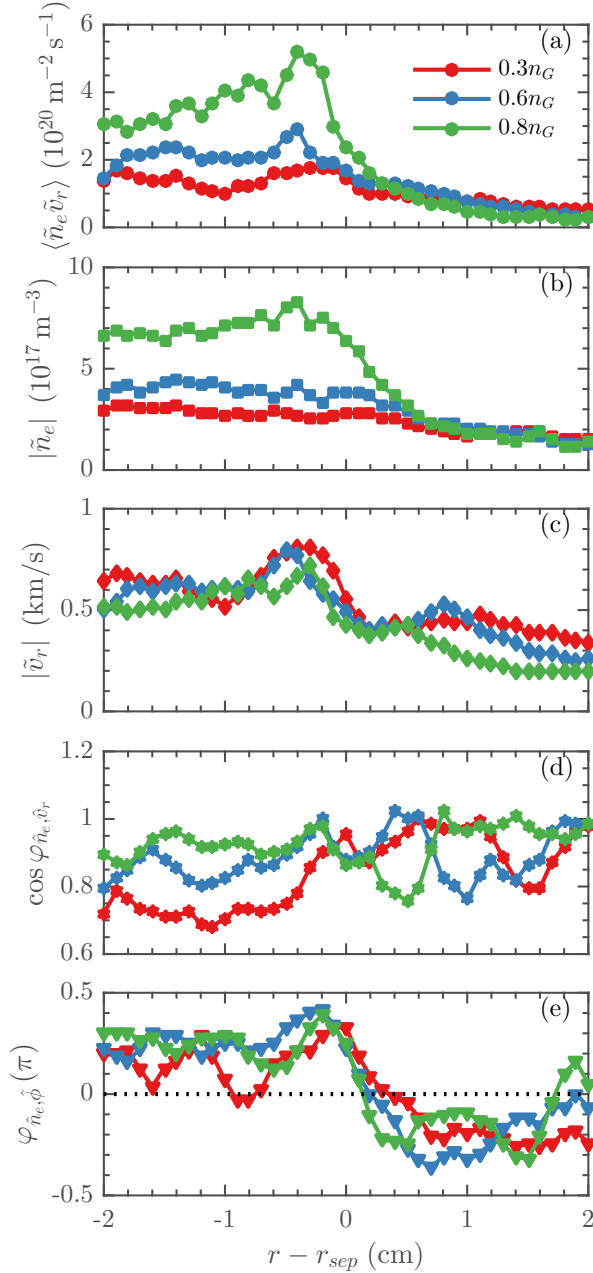


FIG. 11. Radial profiles of electron particle flux (a), RMS of electron density fluctuations (b), RMS of radial velocity fluctuations (c), cross-correlation between velocity and density fluctuations (d), and cross-phase between density and floating potential perturbations (e).

ably, GAMs have greater effective nonlinear growth rate, γ_{NL}^{GAM} , and shearing rate, ω_{GAM} , at higher densities. ω_{GAM} is comparable with the eddy turn-over rate ω_{eddy} , i.e. $\omega_{GAM} \sim \omega_{eddy}$, suggesting GAMs should be able to affect the turbulence dynamics and saturation level. However, ω_{GAM} is still less than mean shearing rate ω_{sh} , i.e. $\omega_{GAM} \sim 0.3 \times \omega_{sh}$. The turbu-

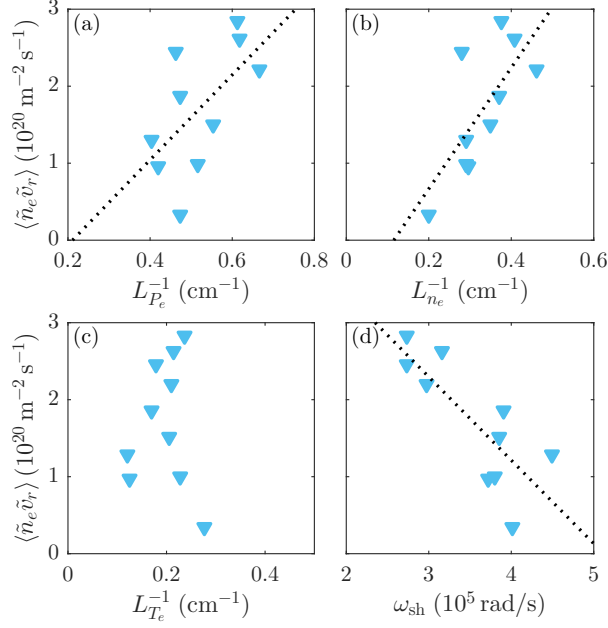


FIG. 12. Averaged particle flux, $\langle \tilde{n}_e \tilde{v}_r \rangle$, inside the separatrix compares against normalized pressure gradient $L_{P_e}^{-1}$ (a), normalized density gradient $L_{n_e}^{-1}$ (b), normalized electron temperature gradient $L_{T_e}^{-1}$ (c), and mean shearing rate of poloidal velocity (d). Black dotted lines imply the linear trends.

lence suppression effect by GAMs is thus less efficient than mean flows.

Besides effects due to shear flows, particle transport can also be altered by the non-adiabatic electron response. The adiabatic parameter, $k_{\parallel}^2 v_{t,e}^2 / \omega \nu_e$, is estimated to drop from about 2 to 0.3, as \bar{n}_e / n_G is raised from 0.3 to 0.8, where $k_{\parallel} \sim 1/qR$ is the parallel wavenumber, $v_{t,e}$ is the electron thermal speed, ν_e is the electron collision rate, and ω is the dominant frequency of turbulence. Such significant change in the adiabatic parameter indicates a possible conversion from *adiabatic* drift waves to *non-adiabatic* resistivity driven modes, e.g. resistive ballooning modes, due to the increased collisionality [16, 18, 20, 40]. These resistive modes have larger fluctuation levels and cross-phase between density and potential perturbations, and therefore produce larger cross-field particle flux and enhance edge cooling. All these processes and their interplay discussed above is summarized in Fig. 15.

In order to obtain steady edge profiles, we employed the shot-by-shot density scans in this study. However, a perturbative study using the density ramp-up or modulation would be necessary to resolve which is first affected by the increased collisionality, the collisional damping of shear flows or the collapse of the Reynolds force (turbulent vorticity flux).

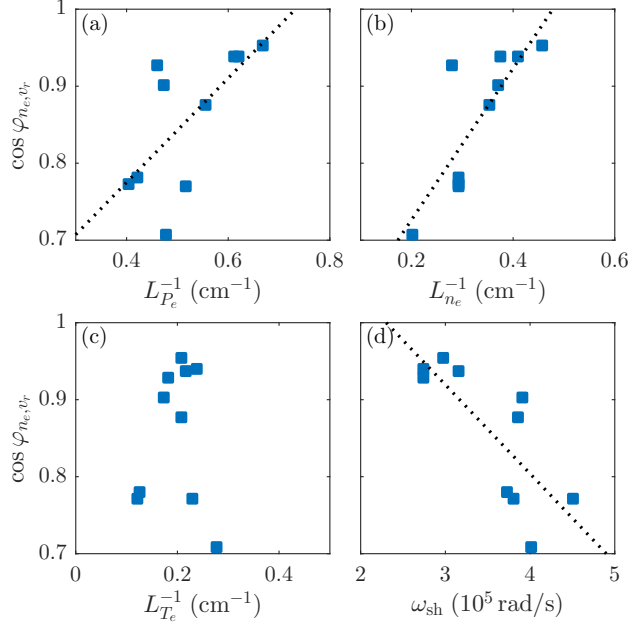


FIG. 13. The averaged cross-correlation, $\langle \cos \varphi_{n_e, v_r} \rangle$, compares against normalized pressure gradient $L_{P_e}^{-1}$ (a), normalized density gradient $L_{n_e}^{-1}$ (b), normalized electron temperature gradient $L_{T_e}^{-1}$ (c), and mean shearing rate of poloidal velocity (d). Black dotted lines imply the linear trends.

B. Link the Enhanced Transport to Radiation Models

Although the enhanced edge transport can explain the decrease of plasma confinement in high collisionality plasmas, the discharges operated near the Greenwald limit are often terminated directly by strong MHD instabilities [2, 4]. As shown in Fig. 16, the enhanced turbulent flux can be incorporated into a schematic of the conventional radiation models, especially the thermo-resistive tearing mode model [12, 14] that gives the dependence on plasma current density. The enhanced particle transport will increase the convective heat flux, $\langle T_e \rangle \langle \tilde{n}_e \tilde{v}_r \rangle$, which dominates the heat loss in plasma boundary regions at higher plasma densities [17], and thus result in strong edge cooling. The edge cooling can increase the resistivity and current density gradient. ∇J then drives tearing modes and hence increase radiation losses, which further decreases the edge temperature. This process iterates until the disruption occurs.

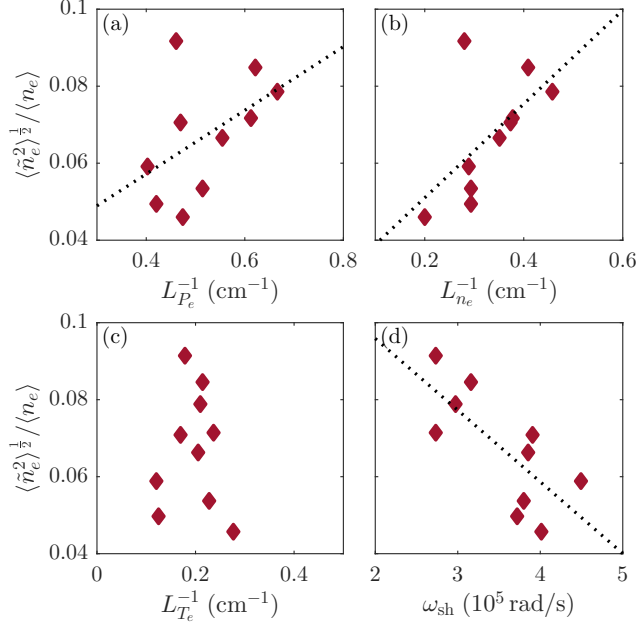


FIG. 14. The normalized RMS of density fluctuations, $\langle \tilde{n}_e^2 \rangle^{1/2} / \langle n_e \rangle$, compares against normalized pressure gradient $L_{P_e}^{-1}$ (a), normalized density gradient $L_{n_e}^{-1}$ (b), normalized electron temperature gradient $L_{T_e}^{-1}$ (c), and mean shearing rate of poloidal velocity (d). Black dotted lines imply the linear trends.

C. Different Behaviors of Zonal Flows and GAMs

The results shown in section III B demonstrate that the low-frequency zonal flow gains less energy from the turbulence at higher densities, and its shearing rate decreases as well. Meanwhile, GAMs gain more energy and thus have higher effective growth rate $\gamma_{\text{NL}}^{\text{GAM}}$ at higher densities, even though the turbulence intensity does not change. Similar observations on GAMs have been reported in a recent investigation from JET [41], in which GAMs amplitudes measured by Doppler backscattering increase as the line-averaged density is raised. The competition between ZFs and GAMs has also been observed in earlier experiments in HL-2A [25] and Alcator C-Mod [42]. In HL-2A's ECRH power scanning experiments, the amplitudes and effective nonlinear growth rates γ_{NL} of ZFs and GAMs were found to increase with the ECRH power, until the ZFs dominate the nonlinear energy transfer process when $P_{\text{ECRH}} \geq 730$ kW [25]. Although some theoretical models [43, 44] have explored the different behaviors of low-frequency ZFs and GAMs, a detailed comparison between the theory and measurements is still lacking. The physics of the coupling between ZFs and GAMs as a

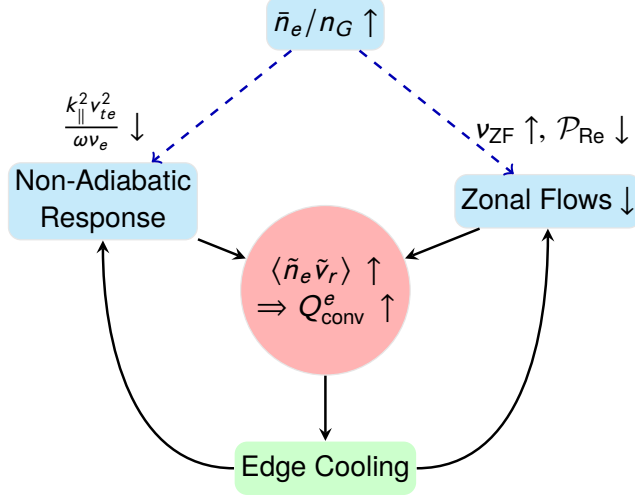


FIG. 15. Sketch of a possible feedback mechanism in high collisionality plasmas. The increased collisionality increases the collisional dissipation of zonal flows, and enhances the correlation between \tilde{n}_e and \tilde{v}_r . Both effects can further enhance turbulent particle flux and edge cooling.

function of the heating power and plasma density remains to be studied.

D. Potential Effect of Magnetic Stress

One topic that deserves further investigation is the effect of magnetic stress, $\langle \tilde{B}_\theta \tilde{B}_r \rangle$, on the driving force for zonal flows near the Greenwald limit. The divergence of the Maxwell stress is known to induce a force on plasmas. The signs of the divergences of the Reynolds stress and magnetic stress are opposite for the drift-Alfvén waves [21, 45], resulting in a lower driving force for the zonal flows in the limit of finite $\hat{\beta}$. As reported in both experiments [18] and numerical simulations [16], electromagnetic fluid drift turbulence grows and becomes the dominant modes controlling edge transport when the density limit is approached.

In present study, the MHD ballooning parameter, $\alpha_{\text{MHD}} = \frac{q^2 R}{L_{Pe}} \beta$ with $\beta = \frac{4\mu_0 P_{e0}}{B^2}$, increases from about 0.1 to 0.3 at the edge as \bar{n}_e/n_G is raised from 0.3 to 0.8. Therefore, magnetic fluctuations are supposed to increase, and their effects on shear flows should be considered. Nonetheless, even without any direct measurement of electromagnetic effects, the reduction in turbulent force for the zonal flows at higher densities suggests that zonal flow is an important element in density limit physics. A probe array that is capable of measuring magnetic and Reynolds stresses has been developed. Direct magnetic stress measurements

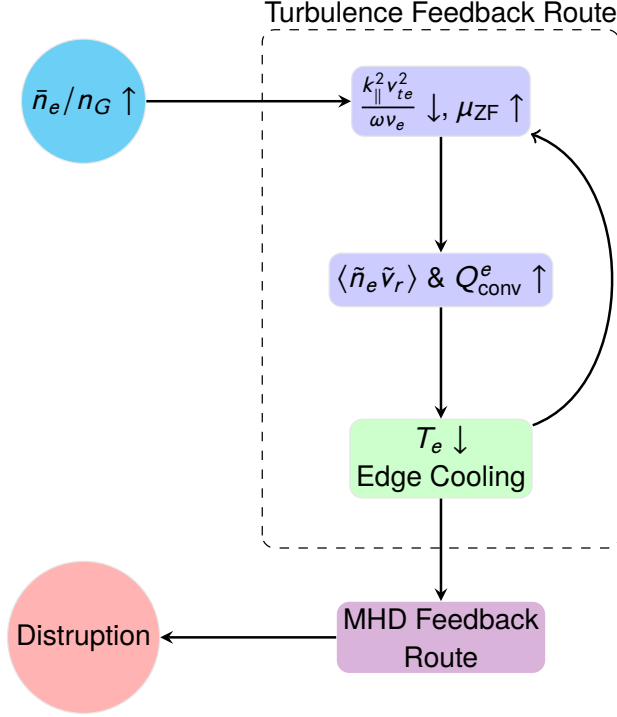


FIG. 16. Schematic of a possible mechanism, which combines the enhanced turbulent transport with MHD radiation models, for disruptions in density limit.

are in progress. We hope to report more results on this topic in the future.

V. SUMMARY

Using a multi-tip Langmuir probe array, edge turbulent particle transport and shear flows have been investigated as the Greenwald limit is approached in the HL-2A tokamak. The results demonstrate that as the line-averaged density increases, the density gradient inside the separatrix increases sharply. The electron temperature profile and poloidal phase velocity of turbulent fluctuations drop as the density increases toward the Greenwald limit. Meanwhile, the low-frequency zonal flow shear and its turbulent drive (Reynolds power) are observed to decrease in high collisionality discharges. Therefore, ZFs cannot regulate turbulent transport. The frequency-resolved nonlinear energy transfer analysis shows that GAMs have larger effective nonlinear growth rate γ_{NL}^{GAM} at higher \bar{n}_e/n_G values. However, ω_{GAM} is still less than the shearing rate of mean flows by a factor of 3–5. Furthermore, the increase of the cross-correlation between \tilde{n}_e and \tilde{v}_r , as well as the amplitude of \tilde{n}_e , results in

substantial enhancement of particle transport in high collisionality plasmas, increasing edge cooling and therefore driving the strong MHD instabilities that lead to disruptions. The adiabatic parameter, $k_{\parallel}^2 v_{t,e}^2 / \omega \nu_e$, drops significantly from about 2 to 0.3 as \bar{n}_e / n_G increases from 0.3 to 0.8. These findings suggest that the increased collisionality may not only damp the low-frequency zonal flow via Coulomb collisions, but also increase the non-adiabatic electron response and hence increase particle transport.

In addition to the poloidal shear flows discussed in present study, the toroidal shear flows can play an important role in mitigating instabilities and improving the plasma confinement. Accordingly, the dynamics of toroidal shear flows and their coupling with poloidal flows in high collisionality plasmas may deserve further explorations.

ACKNOWLEDGMENTS

This work is supported by the Chinese National Fusion Project for ITER under Grant No 2013GB107001, the National Natural Science Foundation of China under Grant Nos 11375053 and 11575055, and the International S&T Cooperation Program of China under Grant No 2015DFA61760.

-
- [1] ITER Physics Expert Group, *Nuclear Fusion* **39**, 2137 (1999).
 - [2] M. Greenwald, *Plasma Physics and Controlled Fusion* **44**, R27 (2002).
 - [3] H. Zohm, C. Angioni, E. Fable, G. Federici, G. Gantenbein, T. Hartmann, K. Lackner, E. Poli, L. Porte, O. Sauter, G. Tardini, D. Ward, and M. Wischmeier, *Nuclear Fusion* **53**, 073019 (2013).
 - [4] M. Greenwald, J. Terry, S. Wolfe, S. Ejima, M. Bell, S. Kaye, and G. Neilson, *Nuclear Fusion* **28**, 2199 (1988).
 - [5] Y. Kamada, N. Hosogane, R. Yoshino, T. Hirayama, and T. Tsunematsu, *Nuclear Fusion* **31**, 1827 (1991).
 - [6] P. Lang, W. Suttrop, E. Belonohy, M. Bernert, R. M. Dermott, R. Fischer, J. Hobirk, O. Kardaun, G. Kocsis, B. Kurzan, M. Maraschek, P. de Marne, A. Mlynek, P. Schneider, J. Schweinzer, J. Stober, T. Szepesi, K. Thomsen, W. Treutterer, E. Wolfrum, and the

- ASDEX Upgrade Team, *Nuclear Fusion* **52**, 023017 (2012).
- [7] M. Mahdavi, T. Osborne, A. Leonard, M. Chu, E. Doyle, M. Fenstermacher, G. McKee, G. Staebler, T. Petrie, M. Wade, S. Allen, J. Boedo, N. Brooks, R. Colchin, T. Evans, C. Greenfield, G. Porter, R. Isler, R. L. Haye, C. Lasnier, R. Maingi, R. Moyer, M. Schaffer, P. Stangeby, J. Watkins, W. West, D. Whyte, and N. Wolf, *Nuclear Fusion* **42**, 52 (2002).
- [8] M. Valovic, J. Rapp, J. G. Cordey, R. Budny, D. C. McDonald, L. Garzotti, A. Kallenbach, M. A. Mahdavi, J. Ongena, V. Parail, G. Saibene, R. Sartori, M. Stamp, O. Sauter, J. Strachan, W. Suttrop, and contributors to the EFDA-JET Workprogramme, *Plasma Physics and Controlled Fusion* **44**, 1911 (2002).
- [9] W. Suttrop, K. Buchl, J. Fuchs, M. Kaufmann, K. Lackner, M. Maraschek, V. Mertens, R. Neu, M. Schittenhelm, M. Sokoll, and H. Zohm, *Nuclear Fusion* **37**, 119 (1997).
- [10] J. Wesson, R. Gill, M. Hugon, F. Schüller, J. Snipes, D. Ward, D. Bartlett, D. Campbell, P. Duperrex, A. Edwards, R. Granetz, N. Gottardi, T. Hender, E. Lazzaro, P. Lomas, N. L. Cardozo, K. Mast, M. Nave, N. Salmon, P. Smeulders, P. Thomas, B. Tubbing, M. Turner, and A. Weller, *Nuclear Fusion* **29**, 641 (1989).
- [11] J. W. Connor and S. You, *Plasma Physics and Controlled Fusion* **44**, 121 (2002).
- [12] D. A. Gates and L. Delgado-Aparicio, *Phys. Rev. Lett.* **108**, 165004 (2012).
- [13] D. Gates, L. Delgado-Aparicio, and R. White, *Nuclear Fusion* **53**, 063008 (2013).
- [14] D. A. Gates, D. P. Brennan, L. Delgado-Aparicio, Q. Teng, and R. B. White, *Physics of Plasmas* **23**, 056113 (2016).
- [15] D. L. Brower, C. X. Yu, R. V. Bravenec, H. Lin, N. C. Luhmann, W. A. Peebles, C. P. Ritz, B. A. Smith, A. J. Wootton, Z. M. Zhang, and S. J. Zhao, *Phys. Rev. Lett.* **67**, 200 (1991).
- [16] B. N. Rogers, J. F. Drake, and A. Zeiler, *Phys. Rev. Lett.* **81**, 4396 (1998).
- [17] B. LaBombard, R. L. Boivin, M. Greenwald, J. Hughes, B. Lipschultz, D. Mossessian, C. S. Pitcher, J. L. Terry, S. J. Zweben, and the Alcator C-Mod Team, *Physics of Plasmas* **8**, 2107 (2001).
- [18] B. LaBombard, J. Hughes, D. Mossessian, M. Greenwald, B. Lipschultz, J. Terry, and the Alcator C-Mod Team, *Nuclear Fusion* **45**, 1658 (2005).
- [19] W. Suttrop, V. Mertens, H. Murmann, J. Neuhauser, J. Schweinzer, and ASDEX-Upgrade Team, *Journal of Nuclear Materials* **266-269**, 118 (1999).
- [20] D. R. Thayer and P. H. Diamond, *Physics of Fluids* **30**, 3724 (1987).

- [21] P. H. Diamond, S.-I. Itoh, K. Itoh, and T. S. Hahm, *Plasma Physics and Controlled Fusion* **47**, R35 (2005).
- [22] A. Fujisawa, *Nuclear Fusion* **49**, 013001 (2009).
- [23] G. R. Tynan, A. Fujisawa, and G. McKee, *Plasma Physics and Controlled Fusion* **51**, 113001 (2009).
- [24] P. Manz, M. Ramisch, and U. Stroth, *Phys. Rev. Lett.* **103**, 165004 (2009).
- [25] M. Xu, G. R. Tynan, P. H. Diamond, P. Manz, C. Holland, N. Fedorczak, S. C. Thakur, J. H. Yu, K. J. Zhao, J. Q. Dong, J. Cheng, W. Y. Hong, L. W. Yan, Q. W. Yang, X. M. Song, Y. Huang, L. Z. Cai, W. L. Zhong, Z. B. Shi, X. T. Ding, X. R. Duan, and Y. Liu (HL-2A team), *Phys. Rev. Lett.* **108**, 245001 (2012).
- [26] M. Xu, G. R. Tynan, P. H. Diamond, C. Holland, J. H. Yu, and Z. Yan, *Phys. Rev. Lett.* **107**, 055003 (2011).
- [27] U. Stroth, P. Manz, and M. Ramisch, *Plasma Physics and Controlled Fusion* **53**, 024006 (2011).
- [28] G. Birkenmeier, M. Ramisch, B. Schmid, and U. Stroth, *Phys. Rev. Lett.* **110**, 145004 (2013).
- [29] I. Cziegler, G. Tynan, P. Diamond, A. Hubbard, J. Hughes, J. Irby, and J. Terry, *Nuclear Fusion* **55**, 083007 (2015).
- [30] I. Cziegler, G. R. Tynan, P. H. Diamond, A. E. Hubbard, J. W. Hughes, J. Irby, and J. L. Terry, *Plasma Physics and Controlled Fusion* **56**, 075013 (2014).
- [31] G. Tynan, M. Xu, P. Diamond, J. Boedo, I. Cziegler, N. Fedorczak, P. Manz, K. Miki, S. Thakur, L. Schmitz, L. Zeng, E. Doyle, G. McKee, Z. Yan, G. Xu, B. Wan, H. Wang, H. Guo, J. Dong, K. Zhao, J. Cheng, W. Hong, and L. Yan, *Nuclear Fusion* **53**, 073053 (2013).
- [32] Z. Yan, G. R. McKee, R. Fonck, P. Gohil, R. J. Groebner, and T. H. Osborne, *Phys. Rev. Lett.* **112**, 125002 (2014).
- [33] G. R. Tynan, I. Cziegler, P. H. Diamond, M. Malkov, A. Hubbard, J. W. Hughes, J. L. Terry, and J. H. Irby, *Plasma Physics and Controlled Fusion* **58**, 044003 (2016).
- [34] Y. Liu, X. Ding, Q. Yang, L. Yan, D. Liu, W. Xuan, L. Chen, X. Song, Z. Cao, J. Zhang, W. Mao, C. Zhou, X. Li, S. Wang, J. Yan, M. Bu, Y. Chen, C. Cui, Z. Cui, Z. Deng, W. Hong, H. Hu, Y. Huang, Z. Kang, B. Li, W. Li, F. Li, G. Li, H. Li, Q. Li, Y. Li, Z. Li, Y. Liu, Z. Liu, C. Luo, X. Mao, Y. Pan, J. Rao, K. Shao, X. Song, M. Wang, M. Wang, Q. Wang, Z. Xiao,

- Y. Xie, L. Yao, L. Yao, Y. Zheng, G. Zhong, Y. Zhou, and C. Pan, *Nuclear Fusion* **45**, S239 (2005).
- [35] X. Duan, X. Ding, J. Dong, L. Yan, Y. Liu, Y. Huang, X. Song, X. Zou, M. Xu, Q. Yang, D. Liu, J. Rao, W. Xuan, L. Chen, W. Mao, Q. Wang, Z. Cao, B. Li, J. Cao, G. Lei, J. Zhang, X. Li, W. Chen, K. Zhao, W. Xiao, C. Chen, D. Kong, M. Isobe, S. Morita, J. Cheng, S. Chen, C. Cui, Z. Cui, W. Deng, Y. Dong, B. Feng, W. Hong, M. Huang, X. Ji, G. Li, H. Li, Q. Li, C. Liu, J. Peng, B. Shi, Y. Wang, L. Yao, L. Yao, D. Yu, L. Yu, B. Yuan, J. Zhou, Y. Zhou, W. Zhong, G. Tynan, P. Diamond, C. Yu, Y. Liu, and the HL-2A Team, *Nuclear Fusion* **53**, 104009 (2013).
- [36] Z. Lin, T. S. Hahm, W. W. Lee, W. M. Tang, and P. H. Diamond, *Phys. Rev. Lett.* **83**, 3645 (1999).
- [37] T. Lan, A. D. Liu, C. X. Yu, L. W. Yan, W. Y. Hong, K. J. Zhao, J. Q. Dong, J. Qian, J. Cheng, D. L. Yu, and Q. W. Yang, *Plasma Physics and Controlled Fusion* **50**, 045002 (2008).
- [38] K. J. Zhao, T. Lan, J. Q. Dong, L. W. Yan, W. Y. Hong, C. X. Yu, A. D. Liu, J. Qian, J. Cheng, D. L. Yu, Q. W. Yang, X. T. Ding, Y. Liu, and C. H. Pan, *Phys. Rev. Lett.* **96**, 255004 (2006).
- [39] M. Xu, G. R. Tynan, C. Holland, Z. Yan, S. H. Muller, and J. H. Yu, *Physics of Plasmas* **17**, 032311 (2010).
- [40] X. Q. Xu, W. M. Nevins, T. D. Rognlien, R. H. Bulmer, M. Greenwald, A. Mahdavi, L. D. Pearlstein, and P. Snyder, *Physics of Plasmas* **10**, 1773 (2003).
- [41] C. Silva, J. Hillesheim, C. Hidalgo, E. Belonohy, E. Delabie, L. Gil, C. Maggi, L. Meneses, E. Solano, M. Tsalas, and J. Contributors, *Nuclear Fusion* **56**, 106026 (2016).
- [42] I. Cziegler, A. E. Hubbard, J. W. Hughes, J. L. Terry, and G. R. Tynan, *Phys. Rev. Lett.* **118**, 105003 (2017).
- [43] K. Miki and P. H. Diamond, *Physics of Plasmas* **17**, 032309 (2010).
- [44] K. Miki and P. Diamond, *Nuclear Fusion* **51**, 103003 (2011).
- [45] R. G. Kleva and P. N. Guzdar, *Physics of Plasmas* **15**, 082307 (2008).